

# A census of $\rho$ -Oph candidate members from *Gaia* DR2

H. Cánovas<sup>1</sup>, C. Cantero<sup>1</sup>, L. Cieza<sup>2</sup>, A. Bombrun<sup>3</sup>, U. Lammers<sup>1</sup>, B. Merín<sup>1</sup>, A. Mora<sup>4</sup>, Á. Ribas<sup>5</sup>, and D. Ruíz-Rodríguez<sup>6</sup>

<sup>1</sup> European Space Astronomy Centre (ESA/ESAC), Operations Department, Villanueva de la Cañada (Madrid), Spain  
e-mail: hcanovas@sciops.esa.int

<sup>2</sup> Núcleo de Astronomía, Facultad de Ingeniería y Ciencias, Universidad Diego Portales, Av. Ejército 441, Santiago, Chile

<sup>3</sup> HE Space Operations B.V. for ESA, European Space Astronomy Centre (ESA/ESAC), Operations Department, Villanueva de la Cañada (Madrid), Spain

<sup>4</sup> Aurora Technology B.V. for ESA, European Space Astronomy Centre (ESA/ESAC), Operations Department, Villanueva de la Cañada (Madrid), Spain

<sup>5</sup> European Southern Observatory (ESO), Alonso de Córdova 3107, Vitacura, Casilla 19001, Santiago de Chile, Chile

<sup>6</sup> Chester F. Carlson Center for Imaging Science, School of Physics & Astronomy, and Laboratory for Multiwavelength Astrophysics, Rochester Institute of Technology, 54 Lomb Memorial Drive, Rochester NY 14623 USA.

February 21, 2019

## ABSTRACT

**Context.**  $\rho$ -Ophiuchus ( $\rho$ -Oph), one of the nearest star forming regions, is an ideal laboratory to study the earlier stages of the stellar and protoplanetary disc evolution. The wealth of accurate astrometric measurements contained in the *Gaia* data release 2 (DR2) can be used to update the census of  $\rho$ -Oph member candidates.

**Aims.** We aim to find potential new members of the  $\rho$ -Oph region and identify those surrounded by a circumstellar disc.

**Methods.** We constructed a control sample composed by 188 bona fide  $\rho$ -Oph members. Using this sample as a reference we applied three different density-based Machine Learning clustering algorithms (DBSCAN, OPTICS, and HDBSCAN) to a sample drawn from the *Gaia* DR2 catalogue centred on the  $\rho$ -Oph cloud. The clustering analysis was applied in the five astrometric dimensions defined by the 3-dimensional Cartesian space and the proper motions in right ascension and declination.

**Results.** The three clustering algorithms systematically identify a main cluster with astrometric properties consistent with those of the control sample. Joining their outcome we constructed a common sample containing 391 member candidates including 166 new (not yet discussed in the literature) objects. Combining the *Gaia* data with 2MASS and WISE photometry we built the spectral energy distributions from 0.5 to 22  $\mu\text{m}$  for the subset of 48 objects with high quality photometry, finding a total of 41 discs (including 11 Class II and 1 Class III new discs).

**Conclusions.** Density-based clustering algorithms are a promising tool to identify candidate members of star forming regions in large astrometric databases. Combining the *Gaia* DR2 data with infrared catalogues it is possible to discover protoplanetary discs that escaped detection by previous surveys. The objects here presented conform an interesting sample to be followed-up with sub-millimetre (and longer wavelengths) observatories and future infrared facilities. If confirmed, the candidate members here discussed would represent an increment of roughly 40 – 50% of the current census of the  $\rho$ -Oph region.

**Key words.** astrometry – methods: data analysis – stars: pre-main sequence – circumstellar matter

## 1. Introduction

Star-forming regions (SFR) composed by hundreds of pre-main sequence (PMS) stars are natural laboratories to learn about the early stages of the stellar evolution process. These places are crucial to study the birth-sites of planets as a significant fraction of the PMS stars is surrounded by a protoplanetary disc. Understanding and identifying the mechanisms driving the evolution of these discs is key to explain how planetary systems are formed (e.g., Morbidelli & Raymond 2016). With this goal in mind several teams have observed large populations of protoplanetary discs in different star forming regions across different wavelengths (e.g., Cieza et al. 2018; Dent et al. 2013; Evans et al. 2009; Haisch et al. 2001). The analysis of extensive disc samples (and their stellar hosts) has revealed trends like the disc mass-stellar mass relation (Andrews et al. 2013; Ansdell et al. 2016; Pascucci et al. 2016) and the decrement of disc mass in mm-sized grains with stellar age (Ansdell et al. 2017; Ruíz-Rodríguez et al. 2018). A general limitation for these studies is

the lack of a complete census of the members of the region under analysis. Such a census is also desirable (among many other reasons) to assess the impact of the environment over the observed disc properties as, for instance, stellar fly-bys are expected to affect the disc sizes, shapes, and masses (Bate 2011, 2018; Cuello et al. 2019).

Identifying the members of any SFR is a difficult task hindered by different causes. Near-by (<400 pc from Earth) regions generally occupy large areas ( $\geq 1\text{deg}^2$ ) on the projected sky, and therefore it is observationally expensive to study them with classical observatories. Furthermore, the late spectral type objects that populate these regions are difficult to detect and characterise due to their intrinsic lower luminosity, and the same applies to any young stellar object (YSO) having a very high extinction. Early works took advantage of the strong X-ray activity and accretion driven  $\text{H}\alpha$  emission of PMS stars to detect them using X-ray observatories and  $\text{H}\alpha$  objective prism surveys (e.g., Montmerle et al. 1983; Walter et al. 1994; Wilking et al. 1987). More

recently, the use of astrometric measurements has made it possible to identify (and/or confirm) hundreds of members of several star forming regions and young associations using different methods (Bruijne 1999; Malo et al. 2013; de Zeeuw et al. 1999). The advent of the *Gaia* mission (Gaia Collaboration et al. 2016) is revolutionising this (and many other) field(s), allowing for the detection of new candidate members of different stellar populations by means of accurate astrometric measurements. In a few remarkable cases, a direct inspection by eye of the *Gaia* astrometry can even reveal the members of a stellar cluster (e.g., the Pleiades example in Brown et al. 2016; Taylor 2017). However, in practise complex algorithms are needed to identify the member candidates based on the astrometric properties of the studied sample (e.g., Gagné et al. 2018). This becomes increasingly difficult when processing large catalogues like the *Gaia* DR2 (Lindgren et al. 2018).

The so-called unsupervised Machine Learning (ML) clustering algorithms are a collection of software tools developed to identify patterns or clusters in *unlabelled* databases. Within these algorithms there are multiple approaches to the problem of cluster detection, like centroid-based algorithms (e.g., the  $k$ -means algorithm, Lloyd 1982), distribution-based clustering (e.g., Gaussian-mixture models), or density-based algorithms (for an overview of clustering analysis in astronomy see e.g., Feigelson & Babu 2012, their Chapter 3.3 and references therein). The latter are well-suited to identify arbitrarily shaped clusters that can be broadly described as overdensities in a lower density space. An advantage of the density-based algorithms is that no prior knowledge about the analysed dataset is needed. In other words, the user does not need to know the amount of clusters present in the dataset, and these algorithms do not assume any particular distribution (like one or multiple Gaussians) when associating the data points to a cluster. The “Density-based spatial clustering of applications with noise” (DBSCAN, Ester et al. 1996) stands out as one of the most famous algorithms in many disciplines, and it is becoming popular in astronomy (e.g., Becari et al. 2018; Bianchini et al. 2018; Caballero & Dinis 2008; Castro-Ginard et al. 2018; Joncour et al. 2018; Hague et al. 2019; Tramacere & Vecchio 2013; Wilkinson et al. 2018). There are a number of modifications and/or improvements of DBSCAN and, among those, the “Ordering points to identify the clustering structure” (OPTICS, Ankerst et al. 1999) and the “Hierarchical density estimates for data clustering, visualisation, and outlier detection” (HDBSCAN, Campello et al. 2013) algorithms are becoming popular due to their recognised performance to detect different types of clusters. However, to date their use in the astronomical literature is still negligible except for a few cases (e.g., Costado et al. 2017; Katz et al. 2017; Kimm et al. 2018; Sans Fuentes et al. 2017).

In this paper we use the DBSCAN, OPTICS, and HDBSCAN algorithms to identify potential members of the  $\rho$ -Oph star forming region in a sample drawn from the *Gaia* DR2 catalogue (Brown et al. 2018).  $\rho$ -Oph, one of the nearest star forming regions to Earth, has been the subject of numerous studies in the past (e.g., Andrews et al. 2009; Andrews & Williams 2007; Cheetham et al. 2015; Cox et al. 2017; Erickson et al. 2011; Mamajek 2008; Wilking et al. 2008). Recently, 289 discs in this cloud have been observed with ALMA aiming to study in detail the different evolutionary stages of the protoplanetary discs (Cieza et al. 2018). Given the youth of this cloud (<5 Myr, see Wilking et al. 2008, and references therein), its members have similar velocity distributions and they are concentrated in a relatively compact region of the Galaxy. In other words, the cloud members should appear *clustered* in the multi-dimensional space defined by their

spatial coordinates and kinematic parameters when compared to the field stellar population. We have applied the clustering algorithms in the 5-dimensional space defined by the 3 spatial coordinates and the 2 kinematic parameters given by the proper motions on right ascension  $\mu_{\alpha^*}$ <sup>1</sup> and declination  $\mu_{\delta}$ . By comparing their results we aim to reduce the selection biases inherent to each algorithm and therefore construct a robust sample of  $\rho$ -Oph members candidates. The samples used for our study are described in Section 2. In Section 3 we describe our methodology and apply the three algorithms to our *Gaia* sample. This section finishes presenting a sample of sources simultaneously identified by the three algorithms. In Section 4 we discuss the properties of this sample, and we use infrared photometry to identify a set of objects showing warm dust emission associated to a circumstellar disc. A summary and conclusions are given in Section 5, while extra figures and tables are shown in the Appendix.

## 2. Sample Construction

### 2.1. The initial sample

We begun by compiling a list of  $\rho$ -Oph member candidates identified as such by means of optical spectroscopy, X-ray emission, and/or Spitzer photometry. To do so we considered the 316 objects listed by Wilking et al. (2008), the sample discussed by Erickson et al. (2011) (135 objects), and the catalogue of  $\rho$ -Oph YSO candidates observed by *Spitzer* during the “Cores to disks” Legacy Program (Evans et al. 2003) and presented by Dunham et al. (2015) (292 objects). The online versions of these catalogues, hosted by the VizieR service, include a SIMBAD (Wenger et al. 2000) ID associated to each object. We used these IDs to obtain the corresponding Two Micron All Sky Survey (2MASS, Skrutskie et al. 2006) IDs. There are not 2MASS counterparts for 2 objects in the Wilking et al. (2008) catalogue, 1 object from Erickson et al. (2011), and 10 objects from Dunham et al. (2015), and these 13 sources are not considered in our study. After accounting for duplicates we obtained our “initial sample”, which contains 465 objects. This sample is listed in Table .1 in the Appendix.

### 2.2. The control sample

With the 2MASS IDs of our initial sample at hand we run an identity cross-match Astronomical Data Query Language (ADQL, Osuna et al. 2008) query between our initial sample and the *Gaia* DR2 catalogue using the 2MASS-*Gaia* matched table (`gaiadr2.tmass_best_neighbour`) available on the *Gaia* archive<sup>2</sup>. This approach is advantageous compared to a sky cross-match by coordinates as there is no need to transform the 2MASS coordinates from the J2000 to the J2015.5 epoch<sup>3</sup>. Our query returned 304 sources. The missing objects are generally fainter at  $J$  band (and therefore probably fainter at  $G$  band) than the detected ones (see Fig. .1 in the Appendix). The results listed on the DR2 catalogue (such as the right ascension  $\alpha$ , the declination  $\delta$ , the parallax  $\varpi$ , and the proper motions in right ascension and declination  $\mu_{\alpha^*}$  and  $\mu_{\delta}$ ) are obtained through a com-

<sup>1</sup>  $\mu_{\alpha^*} = \mu_{\alpha} \cos \delta$ , where  $\mu_{\alpha} = \frac{\alpha_1 - \alpha_2}{\Delta t}$  is the apparent movement in right ascension  $\alpha$  in a given time interval  $\Delta t$  and  $\delta$  is the object declination.

<sup>2</sup> <https://www.cosmos.esa.int/web/gaia/data-release-2>

<sup>3</sup> The astrometric source parameters in the *Gaia* DR2 are referred to the J2015.5 epoch. Across this paper we use the same convention. For a detail description on coordinates transformations see e.g., Sect. 3.1.7 in the *Gaia* DR2 online documentation at <https://gea.esac.esa.int/archive/documentation/GDR2/>

plex data analysis process that relies on treating each observed source as a single, “well behaved” star (the 5-parameter model, see Lindegren et al. 2012, 2018). Binaries and YSOs (which are typically variable and can appear as extended sources at optical wavelengths) can be problematic for the astrometric solution. Therefore, we have applied a selection criteria to extract the sources with high quality astrometry. First, we removed the objects with parallax signal to noise  $\varpi/\sigma_\varpi < 10$  and visibility periods<sup>4</sup>  $\leq 7$  to produce an astrometrically *precise* and *reliable* dataset (see Lindegren et al. 2018; Arenou et al. 2018). Second, we only extracted the sources whose observations are consistent with the 5-parameter model. To do so, we applied the state-of-the-art quality criteria described in the *Gaia* technical note GAIA-C3-TN-LU-LL-124-01<sup>5</sup> that is based on an empirical analysis of the *Gaia* DR2 data. This analysis introduces the re-normalised unit weight error (RUWE), which is a reliable indicator of the goodness-of-fit of the astrometric solution. Using the RUWE as a quality index is specially useful for samples containing very red stars, as the low-mass and extinct PMS stars in  $\rho$ -Oph. We extracted the sources with  $\text{RUWE} < 1.40$  as recommended by this study.

This astrometrically cleaned sample contains 197 objects. We generated its histogram distributions over  $\varpi$ ,  $\mu_{\alpha^*}$ , and  $\mu_\delta$  applying the Bayesian approach derived by Knuth (2006) that optimises the bin widths based on the data distribution and is implemented in *Astropy* (Robitaille et al. 2013). Throughout this paper we use mas and  $\text{mas yr}^{-1}$  as the reference units for the parallaxes and proper motions, respectively, and all the histograms are constructed applying the same methodology. These histograms show bell-shaped distributions with a few objects located far away from the histogram peaks (Fig. .2). We removed these outliers by considering only the objects with  $5 < \varpi < 9$  and  $-20 < \mu_{\alpha^*} < 0$ . The 9 objects excluded by this filter are listed in Table .2 in the Appendix. Given their parallaxes and proper motions we consider them as background objects instead of  $\rho$ -Oph members. Our final sample, hereafter called “control sample”, contains 188 targets. There are *Gaia* radial velocities for 11 of them, with an average value of  $v_{\text{rad}} = 2.6 \pm 13.9 \text{ km s}^{-1}$ . This sample occupies a sky region extending from  $[245.3^\circ : 249.9^\circ]$  in right ascension and  $[-25.4^\circ : -22.9^\circ]$  in declination, and has an average parallax of  $\varpi = 7.1 \pm 0.4$ . The average astrometric properties of the control sample are listed in Table 1 and its parallax and proper motion histograms are shown in the Appendix (Fig. .3). Following Bailer-Jones (2015) we compute the individual distances as  $d = 1/\varpi$  since the parallax fractional error of this sample is lower than 10. This way we obtain an average distance of  $d = 141.2^{+8.4}_{-7.5}$  pc to this sample, where the uncertainty is dominated by the intrinsic dispersion of the dataset. In short, this sample contains 188 bonafide members of the  $\rho$ -Oph cloud that can be used as a reference sample. The control sample members are labelled in Table. .1 with a “Y” in the Control column.

### 2.3. The *Gaia* sample

In order to create a large sample to search for potential new members of  $\rho$ -Oph we run an ADQL cone search on the *Gaia* server centred at  $[247.0^\circ, -24.0^\circ]$  in  $[\alpha, \delta]$  with a search radius of  $r = 3.5^\circ$  chosen to generously encompass the control sam-

<sup>4</sup> As explained in the DR2 archive documentation, a visibility period is a group of observations separated from other groups by 4 or more days. See <http://gea.esac.esa.int/archive/documentation/GDR2/index.html>

<sup>5</sup> see <https://www.cosmos.esa.int/web/gaia/dr2-known-issues> and [http://www.rssd.esa.int/doc\\_fetch.php?id=3757412](http://www.rssd.esa.int/doc_fetch.php?id=3757412)

Stats	$\alpha$ [ $^\circ$ ]	$\delta$ [ $^\circ$ ]	$\varpi$ [mas]	$\mu_{\alpha^*}$ [ $\text{mas yr}^{-1}$ ]	$\mu_\delta$ [ $\text{mas yr}^{-1}$ ]
Mean	246.8	-24.3	7.1	-7.2	-25.5
Sigma	0.6	0.5	0.4	2.0	1.7

**Table 1.** Mean and standard deviation ( $1\sigma$ ) of the control sample.

ple (see Fig. 1). We imposed a parallax range from  $[5 : 9]$  and parallax signal to noise  $\text{SN} > 10$ . This query returned 2814 targets that were reduced to 2300 (including the 188 objects of the control sample) after applying the quality selection criteria described in Sect. 2.2. This sample, labelled hereafter as the “*Gaia* sample”, contains radial velocity values for 236 sources with an average value of  $v_{\text{rad}} = -6.9 \pm 31.8 \text{ km s}^{-1}$ . Figure 2 shows a zoom in of the  $\mu_{\alpha^*}$  vs.  $\mu_\delta$  of the *Gaia* sample, with the control sample overlaid on top as small magenta circles. There is an evident overdensity of sources around the center of the plot. This overdensity seems to contain two different regions or clusters: one with most of its members located around  $[-7.5, -25]$ , and the second one roughly centred at  $[-12, -21]$  in  $[\mu_{\alpha^*}, \mu_\delta]$  (labelled as “Cluster 1” and “Cluster 2” in Fig. 2, respectively). The control sample members are mostly concentrated in Cluster 1.

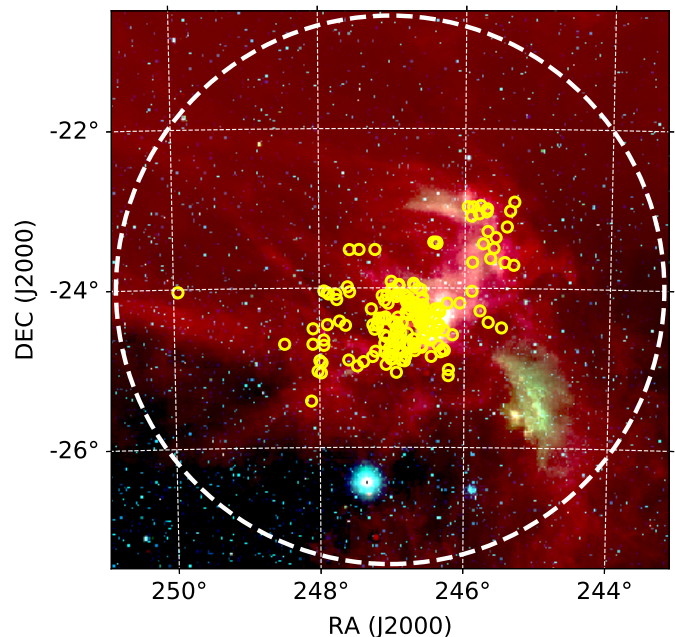


**Fig. 1.** WISE image of the  $\rho$ -Oph region in a square-root stretched scale with RGB colors mapped to 22, 4.6, and 3.4  $\mu\text{m}$ . The control sample is represented as yellow rings. The white dashed ring encompasses the area queried in the *Gaia* server. The saturated blue star towards the south is  $\alpha$  Scorpii (a.k.a. Antares).

## 3. Analysis

### 3.1. Basic concepts of density-based clustering

It is not straightforward to discriminate between the diffuse cluster(s) with no sharp boundaries and the population of back/foreground objects shown in Fig. 2. As mentioned in the introduction, there are multiple software tools able to identify clusters embedded in large databases. We choose to use the family of density-based clustering algorithms because 1) they are specially well suited to detect arbitrarily shaped clusters, and 2)

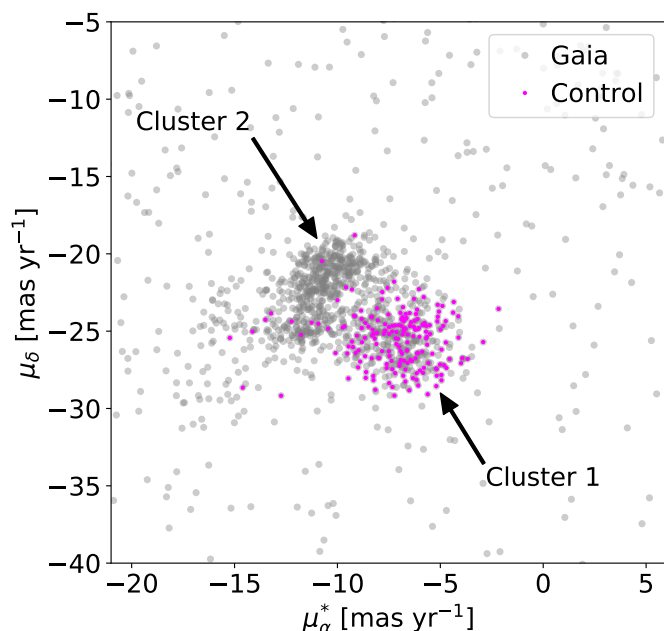


**Fig. 2.** Zoom-in of the proper motions of the *Gaia* sample, represented with grey circles. Their diameter roughly equals the average error on  $\mu_{\alpha^*}$  ( $0.35 \text{ mas yr}^{-1}$ ), which is larger than the average error in  $\mu_{\delta}$  ( $0.23 \text{ mas yr}^{-1}$ ). The control sample is represented as small magenta circles.

by construction these algorithms are not limited to detect clusters having a particular data distribution like e.g. a Gaussian. We have applied and compared three different density-based clustering algorithms: DBSCAN, OPTICS, and HDBSCAN. To date DBSCAN is one of the most popular density-based clustering algorithm and its strong impact on the data mining research community is well recognised<sup>6</sup>. Since its original publication by Ester et al. (1996) several clustering algorithms have been developed aiming to improve its performance and currently there are many options available in the related literature. Here we choose to use the OPTICS and HDBSCAN algorithms because their clustering analysis is based on the hierarchical density structure of the data, which improves the performance of DBSCAN when analysing datasets with strong density gradients. The three algorithms that we use can be freely downloaded from different web repositories that we give in the next subsections.

For our study we considered three spatial and two kinematic dimensions, with the former defined in Cartesian coordinates as

$$X = d \cdot \cos \delta \cos \alpha \quad (1)$$

$$Y = d \cdot \cos \delta \sin \alpha \quad (2)$$

$$Z = d \cdot \sin \delta \quad (3)$$

where  $d$  is the distance computed as the inverse of the parallax. Given the low fraction of objects with radial velocity measurements in our *Gaia* sample we restrict the kinematic dimensions to the proper motions  $\mu_{\alpha^*}$  and  $\mu_{\delta}$ . Before applying the clustering analysis the input dataset must be normalised to ensure that the data dispersion across the processed dimensions is comparable. To do so we used the *Standard Scaler* (with an Euclidean metric) implemented in the Python Machine Learning library scikit-learn (Pedregosa et al. 2011).

In the following lines we introduce the fundamental concepts used by the DBSCAN, OPTICS and HDBSCAN algorithms. Clusters

can be broadly described as localised and arbitrarily shaped regions of an  $N$ -dimensional space with an excess of points per volume unit. In other words, the density in the neighbourhood of each cluster point must exceed some threshold value. The points that do not satisfy this condition do not belong to the cluster and are classified as noise. Two hyperparameters<sup>7</sup> can be used to describe this density threshold:

1.  $\epsilon$  or EPS-distance, which is the distance between two points in the  $N$ -dimensional space, and
2.  $mPts$ , which is the minimum amount of points that are needed to form a cluster.

A cluster can contain core and border points and by definition a cluster must contain at least one core point. The cores are the points having at least  $mPts$  of neighbours within a distance  $d = \epsilon$ . Border points are separated by a distance  $d \leq \epsilon$  from a core point (they are *directly density-reachable*) and have a number of neighbours  $n < mPts$  (i.e., they are less dense than core points). Points separated by distances  $d \gg \epsilon$  belong to the same cluster if they are *density-reachable*, that is, if there is a chain of points  $p_1, \dots, p_n$  such that  $p_{i+1}$  is directly density-reachable from  $p_i$ . Figure 3 illustrates these concepts. Below we present the results of our analysis starting with a basic description of each algorithm. For a thorough description of the clustering algorithms we refer to the specialised literature (e.g., Ankerst et al. 1999; Campello et al. 2015; Ester et al. 1996).

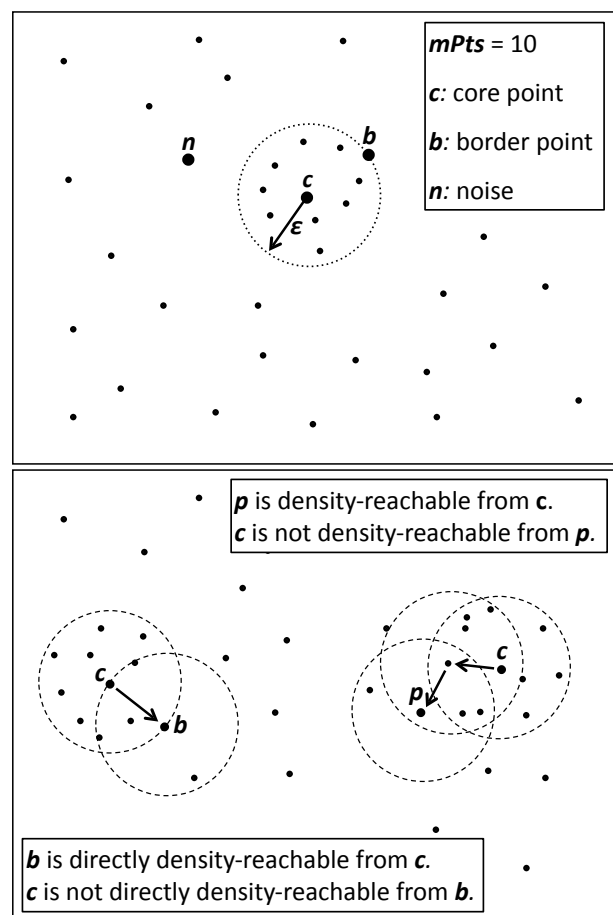


**Fig. 3.** Fundamental concepts used by DBSCAN and OPTICS.

<sup>7</sup> In machine learning jargon these are the parameters specified by the user before the clustering algorithm begins the learning process.

<sup>6</sup> <https://www.kdd.org/News/view/2014-sigkdd-test-of-time-award#>

### 3.2. DBSCAN

DBSCAN<sup>8</sup> is one of the most widely used density-based clustering algorithms. Originally introduced by Ester et al. (1996), it relies in the  $\epsilon$  and  $mPts$  hyperparameters to find arbitrarily shaped clusters of *constant* density. The algorithm results strongly depend on these input parameters and the user may have to select the  $mPts$  and  $\epsilon$  using a trial and error approach.

We begin with the qualitative approach proposed by Ester et al. (1996) to identify optimal  $mPts$  and  $\epsilon$  values to find clusters in the data. Their method consist in inspecting by eye the so-called “sorted  $k$ -distance plot”, which shows the distance to the  $k^{th}$  nearest neighbour (the  $k$ -distance) for each point with all the points sorted out by decreasing  $k$ -distance. By construction, the points that belong to a cluster containing  $k$  members have a lower distance to their closest  $k$ -neighbours than the noise points. Therefore, a compact cluster containing  $n \geq k$  points will create an abrupt decrement in its sorted  $k$ -distance plot. The  $k$ -distance at which the curve reduces again its slope corresponds to the optimal  $\epsilon$  to identify a cluster using  $mPts = k$ . This way, examining these curves for different  $k$  values allows to identify pairs of  $\epsilon$  and  $mPts$  hyperparameters.

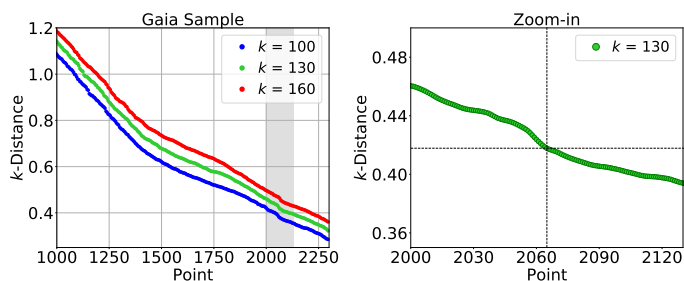


**Fig. 4.** **Left:**  $k$ -distance plots of the *Gaia* sample for different  $k$  (or equivalently  $mPts$ ) values. The grey rectangle encompasses the step-like slope change in the curves (see text). **Right:** Zoom-in of the  $k = 130$  case with the bottom of the step-like slope change indicated by the dashed lines.

We generated a set of  $k$ -distance curves for  $k$  ranging between [80 : 200]. A careful look reveals an step-like slope change located at point  $\sim 2065$  for  $k$  values ranging between [100 : 160], as indicated by the grey shaded region in the left panel of Fig. 4. To find the appropriate  $\epsilon$  values for the different  $k$  values (and equivalently, for different  $mPts$ ) we computed the first and second order derivatives of the sorted  $k$ -distance curves. Given the density distribution of our dataset we had to resample and smooth with a Gaussian kernel the  $k$ -distance curves to isolate the 2<sup>nd</sup>-order derivative maxima, with sampling and smoothing values varying with  $mPts$ . After finding the pairs of  $\epsilon$  and  $mPts$  values for different  $mPts$  we run DBSCAN. The algorithm identifies one single cluster dominated by a population of stars with astrometric distributions consistent with those of our control sample. The results of this exploration for three representative cases and their corresponding histogram distributions in parallaxes and proper motions are listed in Table 2 and presented in Fig. 6 (top row), respectively. The histograms in  $\mu_{\alpha^*}$  show a secondary peak at  $\mu_{\alpha^*} \sim -12.5$  that becomes increasingly significant with  $mPts$ . A similar behaviour is observed in the  $\mu_{\delta}$  distribution, which shows a secondary peak at  $\mu_{\delta} \sim -23$  and is most evident for  $mPts = 100$ . The number of cluster elements varies by  $\sim 10\%$  within the explored range.

### 3.3. OPTICS

By construction, all the clusters found by DBSCAN in a given dataset roughly have the same density. Furthermore, this algorithm struggles to identify all the members in clusters with strong density gradients, such as a cluster composed by a very dense core surrounded by a low density “halo”. The hierarchical clustering algorithm OPTICS<sup>9</sup> (Ankerst et al. 1999) attempts to overcome these issues by focusing on the density-based clustering structure of the data. OPTICS constructs clusters of different density by exploring a range of  $\epsilon$  values and working like an expanded version of DBSCAN.

As a first step, OPTICS finds the densest regions of the cluster and stores this information into two variables named *core distance* and *reachability distance*. The former is the distance from a core point to its closest  $mPts^{th}$  neighbour, and the latter is the smallest distance that makes a point being density-reachable from a core point. For a given value of  $mPts$  OPTICS classifies the points according to their reachability distance from the densest part of the cluster. This is reflected in the so-called “reachability plot” that shows a series of characteristic valleys, each one associated to a potential cluster. The valley-bottom corresponds to the densest cluster region and the valley width roughly scales with the number of cluster elements. The shape of the valley depends on the density distribution of the cluster and the entire dataset. As a second step, OPTICS is executed with the  $mPts$  and  $\epsilon$  hyperparameters derived from the reachability curves as explained below.

Following Ankerst et al. (1999) we explored the reachability curves for  $mPts$  ranging between [10 : 20]. All the curves show a wealth of substructure in the form of multiple local narrow valleys that smoothly disappear with increasing  $mPts$ . The curves also show a main and a secondary (less pronounced) valley (Fig. 5, left panel). We did a first exploration of the two clusters associated to these valleys (see below). The secondary valley is produced by a cluster with  $\sim 180$  elements, with averages  $\bar{\omega} = 6.3 \pm 0.2$ ,  $\bar{\mu}_{\alpha^*} = -10.6 \pm 1.2$ , and  $\bar{\mu}_{\delta} = -21.4 \pm 1.4$ . Its members are part of the “Cluster 2” shown in Fig. 2 and only one of the control sample members is part of it. The average astrometric properties (including the spatial distribution) of this secondary cluster are different from those of the control sample and therefore we defer a detailed analysis of this cluster to a separate and dedicated study. In what follows we focus our discussion on the main valley and its associated cluster, as this one has astrometric properties similar to those of the control sample. In the explored range the shape of the valley is similar to the “case B” described by Ankerst et al. (1999) in their Sect. 4.3 (see also their Figs. 17 and 18). The valley shows a local plateau at its beginning (labelled as Starting of the cluster, SoC) that has similar y-coordinates as the cluster end (which appears as an abrupt decrement in the curve and is labelled as Reachability end). This is illustrated in the right panel of Fig. 5. In this case, the appropriate  $\epsilon$  to extract the cluster for  $mPts = 16$  corresponds to the y-coordinates of the Reachability end, that is,  $\epsilon = 0.259$ . The beginning and end of the main valley are clearly detected for  $mPts$  ranging between [14 : 18], and therefore we restrict our analysis to this range. This way we derived the  $\epsilon$  values for the corresponding  $mPts$  and then executed OPTICS using these hyperparameters. As representative cases we consider the ones where the Reachability end is clearly detected. Those are listed in Table 2, and their corresponding histograms in parallax and proper motions are shown in Fig. 6 (central row). All the cases produce a similar outcome with a variation in cluster elements

<sup>8</sup> We use the scikit implementation by Pedregosa et al. (2011).

<sup>9</sup> We use the pyclustering (v0.8.1) implementation by Novikov (2018).

$< 10\%$ . The histogram distributions show a secondary peak at  $\mu_{\alpha^*} \sim -12.5$  and  $\mu_{\delta} \sim -23$ .

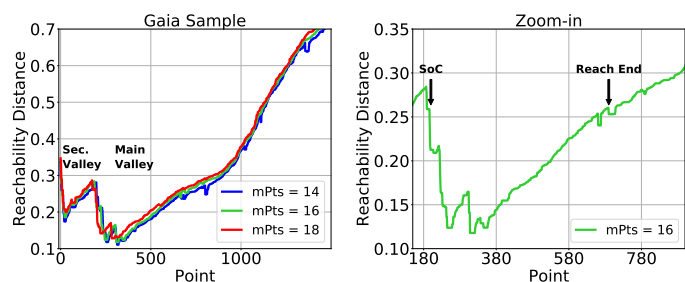


**Fig. 5.** Left: Reachability distance plots of the *Gaia* sample computed for a range of *mPts*. Right: Zoom-in of the *mPts* = 16 case, highlighting the location of the first and last points of the main valley.

### 3.4. HDBSCAN

A drawback of both DBSCAN and OPTICS is the potential difficulty in finding optimal  $\epsilon$  and *mPts* values. In high-density datasets it can be complicated to unambiguously identify the step-like slope change in the *k*-distance curves used by DBSCAN and the first/last points of the valleys in the reachability-distance plots generated by OPTICS. The hierarchical algorithm HDBSCAN<sup>10</sup> (Campello et al. 2013, 2015) requires one single hyperparameter to operate (the “minimum cluster size” *mCls*, conceptually similar to *mPts*), and it therefore simplifies the task of finding appropriate hyperparameters. As OPTICS, HDBSCAN can identify clusters with different densities and it is sensitive to the density gradients inside a cluster.

HDBSCAN is much more complex than DBSCAN and OPTICS and therefore we just briefly describe its main steps, referring to Campello et al. (2015) for a thorough description of the algorithm. First, the low-density and noise points are identified by computing the *mutual reachability-distance*. This quantity is the maximum of three distances for each pair of data points *A* and *B*: the core distance to the *k*<sup>th</sup> point for *A* and *B*, and the metric distance between *A* and *B*. Second, HDBSCAN uses the mutual reachability distance to identify and classify the densest points of the dataset according to their relative density. The points are grouped into clusters through a multi-stage process that involves generating the minimum spanning tree of the mutual reachability-distances, computing the data points density hierarchy, and creating a hierarchical condensed cluster tree. Apart from identifying the clusters in a given dataset, HDBSCAN uses the condensed cluster tree to assign a membership probability to each member of a cluster.

We set the probability threshold to the maximum (i.e. we only considered cluster members with 100% associated membership probability) and then explored the range of *mCls* values from [20 : 100]. For *mCls* > 58 HDBSCAN does not find any cluster, while for *mCls* between [20 : 58] the algorithm systematically identifies a main and a secondary cluster. After a first exploration we find that the secondary cluster has between 30 and 50 elements (none of them included in the control sample) and, as with OPTICS, it has proper motions consistent with those of Cluster 2 in Fig. 2 (with averages  $\varpi = 6.3 \pm 0.1$ ,  $\mu_{\alpha^*} = -10.7 \pm 0.9$ , and  $\mu_{\delta} = -21.3 \pm 1.3$ ). As explained before, in this paper we focus our attention on the main cluster found by HDBSCAN because its astrometric properties are consistent with those of the control sample. For *mCls* ranging from [20 : 58]

<sup>10</sup> We use the implementation by McInnes et al. (2017).

the number of cluster members mostly oscillates around 460. As representative outputs we consider those listed in Table 2 as, excluding a few cases with number of elements < 200, those encompass the minimum, maximum, and roughly average number of elements of the main cluster. The corresponding histograms are shown in Fig. 6 (bottom row). The proper motion distributions show two secondary peaks at  $\sim -12.5$  in  $\mu_{\alpha^*}$  and  $\sim -23$  in  $\mu_{\delta}$ , albeit these peaks are less pronounced than in the DBSCAN and OPTICS cases.

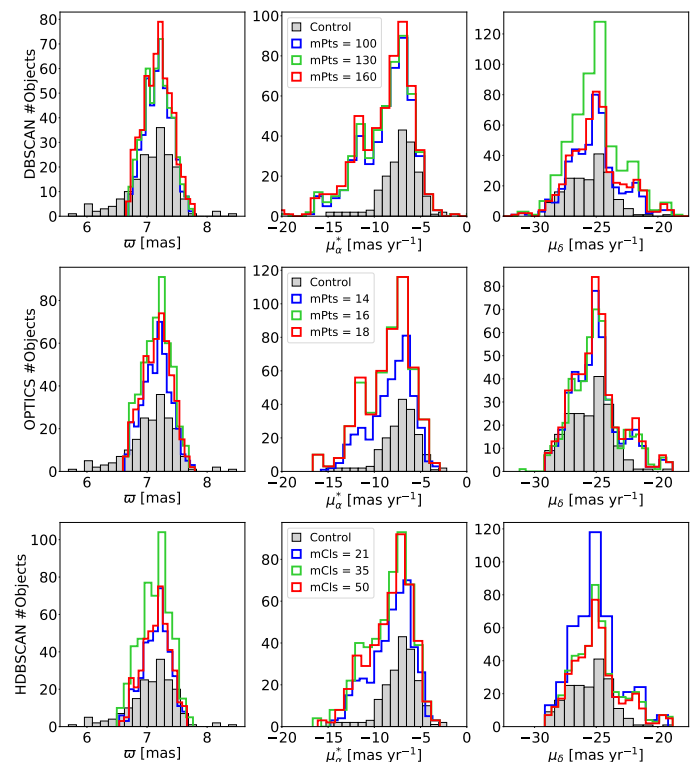


**Fig. 6.** Histogram distributions of the cluster identified by DBSCAN (top) and the main cluster identified by OPTICS (center) and HDBSCAN (bottom) for different hyperparameters (see legend and Table 2). The control sample is represented with grey bars.

Algorithm	<i>mPts</i>	<i>Eps</i>	Elements	Control (%)
DBSCAN	100	0.373	492	155 (82.4)
DBSCAN	130	0.418	524	156 (83.0)
DBSCAN	160	0.455	552	158 (84.0)
OPTICS	14	0.245	451	157 (83.5)
OPTICS	16	0.259	494	157 (83.5)
OPTICS	18	0.265	497	159 (84.6)
HDBSCAN	21	–	427	153 (81.4)
HDBSCAN	35	–	502	163 (86.7)
HDBSCAN	50	–	462	158 (84.0)

**Table 2.** Explored hyperparameters and number of cluster elements identified by each algorithm. The fifth column indicates the number of control sample members found, with the percentage indicated inside a parenthesis. For HDBSCAN the first column corresponds to the *mCls*.

### 3.5. The common sample

The three algorithms previously discussed find a population of objects with astrometric properties (excluding the yet unknown

radial velocity) consistent with those of the control sample. However, the algorithm outputs are slightly different and the cluster size is sensitive to the chosen algorithm and corresponding hyperparameters (see Table 2). It is therefore not straightforward to decide which algorithm and hyperparameter combination produces the most reliable sample of potential  $\rho$ -Oph members. To overcome this difficulty we have merged the results listed on Table 2, conservatively choosing the cluster combination that produces the smaller output in terms of elements. That is, we combine the DBSCAN output obtained for  $mPts = 100$ , the OPTICS output with  $mPts = 14$ , and the HDBSCAN output with  $mCls = 21$ . After accounting for duplicates the merged cluster (labelled hereafter as “combined sample”) contains 532 sources, 164 of them included in the control sample. In this cluster there are 59 sources only detected by DBSCAN, and 13 sources detected only by OPTICS and other 13 only by HDBSCAN. Table 3 lists the members of this sample and includes a column labelled as “DOH” (acronym for DBSCAN-OPTICS-HDBSCAN) that indicates the algorithm(s) that detect each member using a “Y/N” nomenclature. For example, if a source is detected only by DBSCAN its DOH value is “YNN”, while a member detected by OPTICS and HDBSCAN has DOH=“NYY”. From this combined sample we extracted the sources simultaneously identified by the 3 algorithms (i.e., those with DOH=“YYY”). Hereafter we focus our analysis on this common sample that contains 391 sources, 148 of them belonging to the control sample.

The common sample contains 243 potential Ophiuchus member candidates that were not included in the three catalogues used to construct the control sample described in Sect. 2.2. In order to gather further information about these sources we queried the SIMBAD database using as identifier the *Gaia* DR2 source\_id. This query returned 77 objects, that is, to date 166 objects in our common sample do not appear linked to any publication according to the SIMBAD service. Combining the results obtained by Kraus & Hillenbrand (2007), Luhman & Mamajek (2012), and Rizzuto et al. (2015), we find that 43 targets out of the 77 known objects have been associated to the Upper Scorpius subgroup of the Scorpius-Centaurus OB association.

## 4. Results

### 4.1. Astrometric properties

The sky-projected distribution of the common sample is shown in Fig. 7 on top of the extinction map produced by the COMPLETE project (Ridge et al. 2006) applying the NICER algorithm (Lombardi & Alves 2001) to 2MASS observations. Nearly 1/3 of the common sample objects (125 sources) are found within a distance  $r \leq 0.6^\circ$  from the extinction peak (roughly at  $\alpha, \delta = 246.7^\circ, -24.5^\circ$ ) of the main dark cloud of Ophiuchus, the Lynds 1688 dark cloud (L1688, see e.g., Wilking et al. 2008). Most of these objects (113) are also included in the control sample. The apparent lack of sources at the innermost core of this cloud is most likely a consequence of the very high extinction exceeding  $A_V > 20$  at this location. We do not find a significant correlation between the distances to each object (indicated by the rainbow color bar) and the sky-projected location of the sample.

Figure 8 shows the proper motions of the common sample (plotted as small cyan circles) on top of the zoomed-in distributions of the *Gaia* sample (as grey circles). As in Fig. 2, the diameter of the grey circles equals the average error on  $\mu_{\alpha^*}$  of the *Gaia* sample. The 40 control sample sources not included in the common sample are plotted as small magenta circles. Most of the common sample members are concentrated around the ap-

parent cluster located at higher  $\mu_{\alpha^*}$  values (labelled as “Cluster 1” in Fig. 2), but a non negligible fraction of them are also found in the apparent cluster located towards higher  $\mu_\delta$  and lower  $\mu_{\alpha^*}$  values (“Cluster 2” in Fig. 2). The parallax and proper motion histograms of the common sample are shown in Fig 9. The three distributions deviate from a single bell-shaped distribution and the parallax histogram shows two separate peaks at  $\varpi = 7.0$  and  $\varpi = 7.2$ . The parallax distribution is narrower than the control sample counterpart ( $\varpi \in [6.7 : 7.7]$  versus  $\varpi \in [5.7 : 8.5]$ ). Computing the distance as the inverse of the parallax we obtain an average distance of  $d = 139.4^{+4.1}_{-3.8}$  pc to the common sample. The difference in parallax ranges means that the common sample members are distributed in a localised spatial region with distances ranging from [130 : 150] pc, whereas the control sample occupies a spatial region with distances ranging between [118 : 176] pc. The proper motion histograms show a secondary peak or shoulder at  $\mu_{\alpha^*} \sim -12$  and  $\mu_\delta \sim -21$ , as expected from Fig. 8. We fitted a combination of two Gaussian profiles to the  $\mu_{\alpha^*}$  and  $\mu_\delta$  distributions using a Levenberg-Marquardt algorithm (the fit did not converge for the parallax distribution). The fits are shown as a solid (combined fit), dashed (main Gaussian) and dotted (secondary Gaussian) lines on top of the histograms in Fig. 9. The mean and Full Width at Half Maximum (FWHM) of the Gaussian fits and the average astrometric properties of the common sample are listed on Tables 4 and 5, respectively.

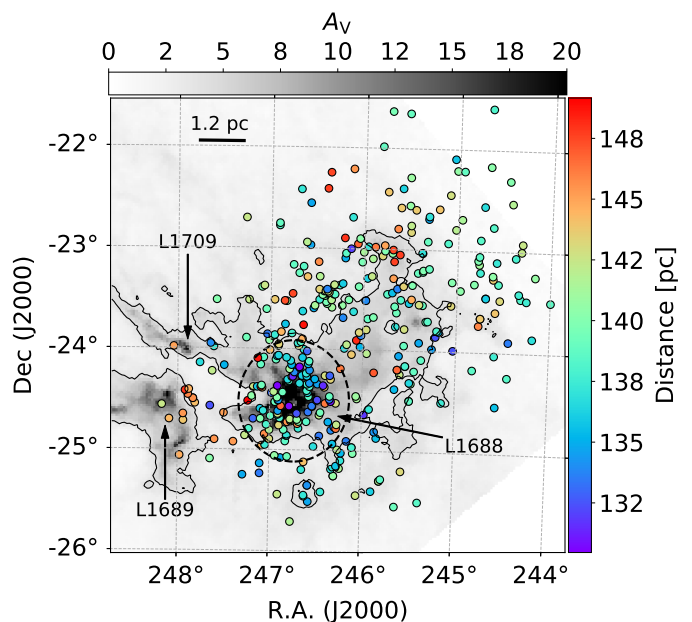


**Fig. 7.** The common sample overlaid on top of an extinction map. The contour delimitates the  $A_V = 4$  regions. The arrows indicate the location of the main Lynds dark clouds in this area, while the black dashed line encompasses the  $r \leq 0.6^\circ$  region centred on the extinction peak. The size scale is calibrated for the average distance to the common sample.

### 4.2. Color Magnitude Diagram

Fundamental properties like stellar masses or ages can be estimated from a Color Magnitude Diagram (CMD), if the extinction for each object is known. There are photometric measurements for all the objects in our common sample in the three *Gaia* bands (broad  $G$  and the two narrower  $G_{BP}$  and  $G_{RP}$ , Brown et al. 2018) bands, but the extinction is estimated for only 95 of them, with an average value of  $A_G = 1.7 \pm 0.6$ . As noted by Andrae et al. (2018) the *Gaia* extinctions are not accurate at the indi-

$\alpha$ [deg]	$\delta$ [deg]	$\varpi$ [mas]	$\mu_{\alpha^*}$ [mas yr $^{-1}$ ]	$\mu_{\delta}$ [mas yr $^{-1}$ ]	source_id	Control	DOH
243.3719939	-23.1855471	7.2072955	-8.8893582	-25.4157242	6242554649124043520	N	YNN
243.7959809	-23.3786153	7.1327026	-15.5389965	-24.4785008	6050385511522948096	N	YNN
243.8016470	-23.3127069	7.1572953	-8.8631422	-26.3450177	6050388913137070848	N	YNY
243.8311704	-25.6701140	7.4134597	-9.1980374	-27.1873024	6048740710844628864	N	YNN
243.8642421	-22.6577711	7.1951507	-10.8897003	-24.8620069	6242599763466335104	N	YNY

**Table 3.** First 5 entries of the combined sample (532 members) described in Sect. 3.5. The sixth column is *Gaia* DR2 source\_id. The entire table is provided in the electronic version of this article. The “Control” column indicates if a target is part of the control sample following a Yes/No nomenclature. All the coordinates are given in J2015.5 epoch (as in *Gaia* DR2).

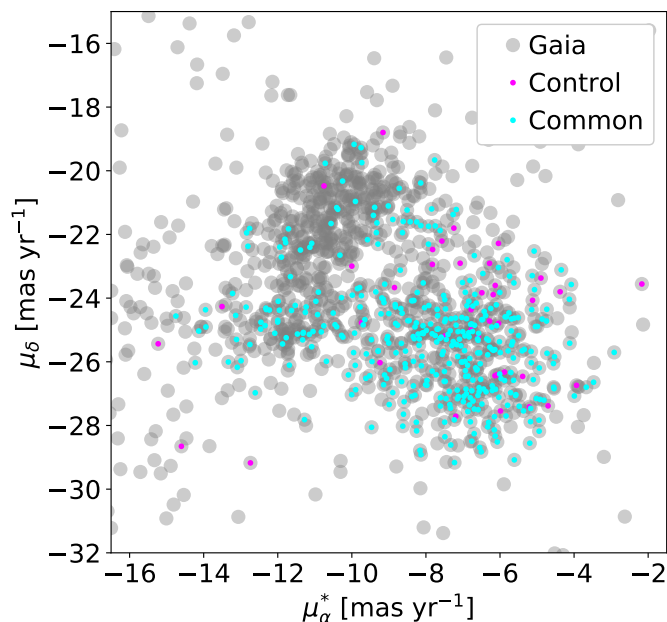


**Fig. 8.** Same as Fig. 2, including the common sample as cyan small circles. The 40 sources from control sample not included in the common sample are shown as small magenta circles.

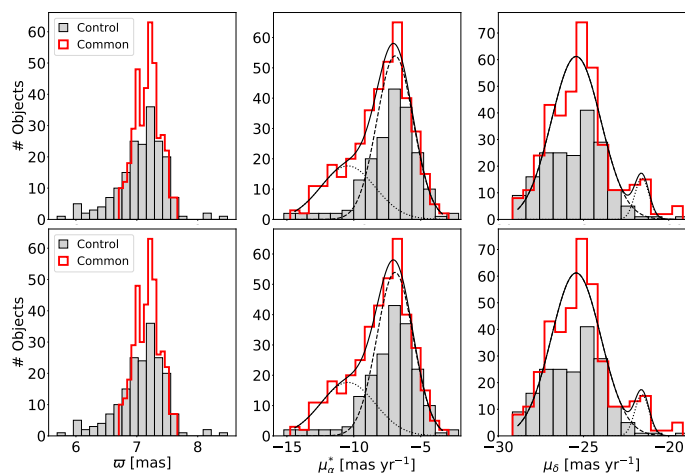


**Fig. 9.** Histogram distributions of the common sample (see Sect. 3.5). A two-Gaussian fit is shown as a solid line on top of the proper motion histograms.

vidual star level. Most importantly for our particular case, the effective temperatures and extinctions listed on the *Gaia* DR2 are based on a naked stellar model that does not include the con-

	$\mu_{\alpha^*}$ [mas yr $^{-1}$ ]	$\mu_{\delta}$ [mas yr $^{-1}$ ]
Mean	$-6.9 \pm 0.1$	$-25.4 \pm 0.1$
FWHM	$3.2 \pm 0.1$	$3.4 \pm 0.1$
Mean	$-10.4 \pm 0.5$	$-21.6 \pm 0.1$
FWHM	$4.8 \pm 0.8$	$1.0 \pm 0.4$

**Table 4.** Mean and FWHM of the Gaussian fits shown in Fig. 9 for the main and secondary Gaussians (upper and lower halves, respectively). The errors are the  $1\sigma$  uncertainties of the fit.

	$\alpha$ [ $^{\circ}$ ]	$\delta$ [ $^{\circ}$ ]	$\varpi$ [mas]	$\mu_{\alpha^*}$ [mas yr $^{-1}$ ]	$\mu_{\delta}$ [mas yr $^{-1}$ ]
Mean	246.2	-23.9	7.2	-8.0	-25.2
Sigma	0.8	0.8	0.2	2.2	1.9

**Table 5.** Mean and standard deviation ( $1\sigma$ ) of the common sample across different dimensions.

tribution from the dust in the star forming region and/or the protoplanetary discs that probably surround and important fraction of the common sample sources. Therefore we looked for published extinction values of our sources. Dunham et al. (2015) give extinction values in the V band,  $A_V$ , for 83 objects with an average value of  $A_V = 6.0 \pm 4.0$ . Rizzuto et al. (2015) estimate  $A_V$  for other 20 objects, with an average of  $A_V = 0.9 \pm 0.6$ . The large difference between both studies is due to the fact that, by construction, the sample by Dunham et al. (2015) is composed by YSOs surrounded by discs, while the sample discussed by Rizzuto et al. (2015) is dominated by objects without detected discs. Combining both studies we obtain  $A_V$  estimates for 26% of the sources in the common sample, with an average extinction of  $A_V = 5.0 \pm 4.1$ . Using the *Gaia* DR2 extinction coefficients listed in the Filter Profile Service provided by the Spanish Virtual Observatory (SVO<sup>11</sup>, Rodrigo et al. 2012) this average value translates into  $A_G = 4.7$ . As the individual extinctions for most of the sources remain unknown to date, we opted for constructing an extinction uncorrected CMD. For this purpose we used the *G* and *G<sub>RP</sub>* bands, as their characteristic error is lower than in the *G<sub>BP</sub>* band (for our entire sample we obtain a  $\delta G$ ,  $\delta G_{RP}$ , and  $\delta G_{BP}$  of 0.002, 0.007, and 0.04 mags, respectively). We used the individual parallaxes to compute the absolute magnitudes for each source as  $M = m + 5(\log_{10} \varpi + 1)$ . To have a rough idea of the extinction effect we computed the extinction vector using the previously mentioned average  $A_G$ . Figure 10 shows the obtained diagram, with the common sample plotted as small cyan

<sup>11</sup> <https://svo.cab.inta-csic.es/main/index.php>

circles on top of the grey circles that represent the *Gaia* sample. As in Fig. 8, the 40 sources that belong to the control sample but that are not included in the common sample are shown as magenta small circles. Except for a few objects, the common sample occupies a separate region in this plot, as expected if this sample is significantly younger than the rest of the stars in the *Gaia* sample. Given the high extinction of the  $\rho$ -Oph region the common sample is most likely composed of objects located in the near side of the cloud surface, as those in the inner regions of the cloud are probably too obscured to be detected by *Gaia*. Median ages for  $\rho$ -Oph members at the cloud surface range from 2 to 5 Myr (Wilking et al. 2008). To put our sample in context we gathered the BT-Settle/CIFIST (Baraffe et al. 2015) and Parsec (Marigo et al. 2017) stellar evolutionary models for stellar masses below and above  $1.4 M_{\odot}$ , respectively. The 2 and 5 Myr isochrones drawn from these models are shown as a solid and a dashed blue line on top of the CMD, respectively, while the evolutionary tracks for three different stellar masses (0.1, 0.5, and  $1.4 M_{\odot}$ ) are indicated by orange thick lines. Most of the common sample objects are located above the isochrone. Similarly, the bulk of the common sample ( $\sim 91\%$  of it) lies below the  $0.1 M_{\odot}$  evolutionary track.

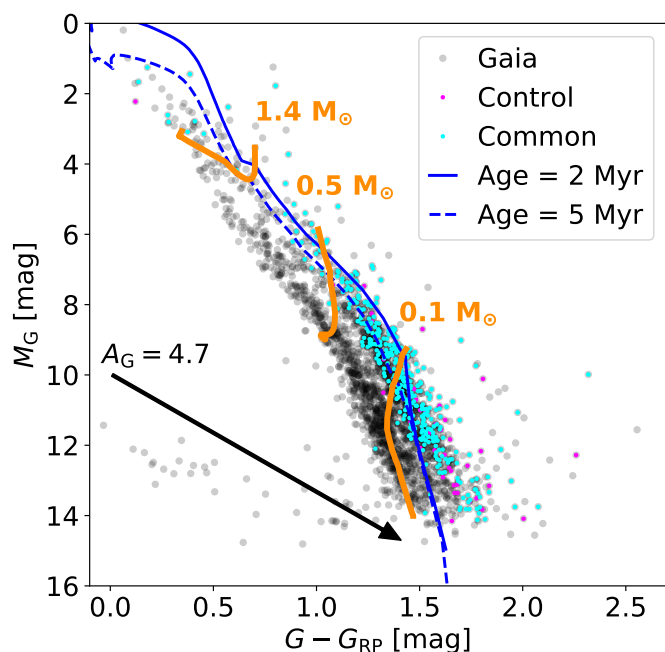


**Fig. 10.** Color Magnitude Diagram. The control sample sources not included in the common sample are shown as small magenta circles. The diameter of the black circles is larger than the average photometric error. The extinction vector is computed for the average  $A_G$  derived from a subset of sources (see Sect. 4.2).

#### 4.3. Potential discs

Given the youth of  $\rho$ -Oph, a large fraction of our common sample members might be surrounded by a protoplanetary disc. The presence of such a disc as well as its evolutionary stage can be inferred from the warm dust emission at infrared wavelengths. In order to obtain the near infrared photometry for the common sample sources we used the crossmatched tables provided by the *Gaia* consortium (available in the *Gaia* archive) `gaiadr1.tmass_original_valid` and `gaiadr2.tmass_best_neighbour`. Combining

these two tables we retrieved the 2MASS photometry for 382 sources. We then repeated the same procedure but using the `gaiadr2.allwise_best_neighbour` and `gaiadr1.allwise_original_valid` tables to obtain the mid infrared photometry measured by the Wide-Field Infrared Survey Explorer (WISE, Wright et al. 2010), retrieving observations for 332 sources. All the retrieved 2MASS photometry has quality flag “A” at the 3 bands, but this is not the case for the WISE photometry. Therefore, before combining these outputs we disregarded the objects with photometric quality flag different than “A” or “B” at any of the WISE bands. Furthermore, we only considered objects with contamination and confusion flag (c $\overline{f}$ ) equal to “0” in all WISE bands, and with extended source flag (ex) lower than 2. At this stage, we inspected by eye the WISE images of every source to remove those affected by artefacts. The WISE band 4 photometry can be strongly affected by background emission which might be mistakenly associated to the warm dust emission produced by a circumstellar disc (Kennedy & Wyatt 2012). To minimise this potential confusion we used the `Astropy/photutils` package to perform aperture photometry to measure the signal to noise at the peak of the WISE band 4 image of each source. We used an aperture mask with radius  $r_{\text{ap}} = 12''$  to measure the peak emission and a sky aperture ring of  $r_{\text{in}} = 20''$  and  $r_{\text{out}} = 25''$  to estimate the background signal, with both apertures centred on the *Gaia* DR2 coordinates ( $\alpha$  and  $\delta$ ) for each source. We filtered out all the sources with peak emission S/N  $\leq 4$ . Applying this selection criteria we finally obtained a sample of 48 sources (25 of them belonging to the control sample) with 2MASS and WISE photometry.

We combined the *Gaia* photometry with the infrared photometry to build up the Spectral Energy Distributions (SEDs) for the 48 sources previously selected. To convert from magnitudes to flux units (Jy) we retrieved the effective wavelengths and zero points (ZP) for each photometric band from the SVO. The total uncertainty of the fluxes was computed as the quadratic sum of the errors associated to the photometric extraction process, the ZP, and the systematic errors. The *Gaia* photometric uncertainties are negligible compared to those from the 2MASS and WISE. The largest source of uncertainties are the systematic errors associated to the WISE photometry, which is tied to the Spitzer photometric calibration (Jarrett et al. 2011). Here we adopt an absolute calibration uncertainty of 5% for the W1, W2, and W3 bands, and 10% for the W4 band. Given the broad wavelength coverage of the WISE filters, a color correction must be applied when transforming magnitudes to fluxes. For each source we computed the  $\alpha$  flux slope ( $F_{\nu} \sim \nu^{\alpha}$ ) for the different WISE bands and then applied the correction factors following Section VI of the “Explanatory Supplement to the WISE All-Sky Data Release Products<sup>12</sup>”.

Traditionally, the protoplanetary discs have been classified according to the infrared slope of their SED defined as

$$\alpha_{\text{IR}} = \frac{\log(\lambda_1 F_{\lambda_1}) - \log(\lambda_0 F_{\lambda_0})}{\log(\lambda_1) - \log(\lambda_0)}, \quad (4)$$

where  $\lambda_1$  and  $\lambda_0$  correspond to  $\sim 2$  and  $\sim 22 \mu\text{m}$  (Lada & Wilking 1984; Lada 1987). This way, objects with  $\alpha_{\text{IR}} > 0.3$  (i.e., those with a raising SED towards the mid-infrared) are labelled as Class I and are associated to young stellar objects surrounded by a primordial envelope and massive, little evolved disc. Objects with  $-0.3 > \alpha_{\text{IR}} > -1.6$  are classified as Class II sources and represent a more evolved stage during the disc

<sup>12</sup> [http://wise2.ipac.caltech.edu/docs/release/allsky/expsup/sec4\\_4h.html](http://wise2.ipac.caltech.edu/docs/release/allsky/expsup/sec4_4h.html)

evolution, while those with  $0.3 > \alpha_{\text{IR}} > -0.3$  are classified as Flat SED sources and show intermediate properties between the Class I and II stages (Greene et al. 1994). Objects with  $\alpha_{\text{IR}} < -1.6$  are classified as Class III and they are associated to tenuous discs. Applying this criteria and using the  $K_s$  ( $\lambda_{\text{eff}} \sim 2.2 \mu\text{m}$ ) and W4 ( $\lambda_{\text{eff}} \sim 22.1 \mu\text{m}$ ) bands we find 36 Class II and 12 Class III objects within the 48 objects with infrared photometry contained in the common sample. This traditional classification is useful and allows for the comparison with previous works, but it has some limitations (see e.g., Cieza et al. 2007; Merín et al. 2010). In particular, as already noted by Evans et al. (2009), the Class III encompasses two different types of objects: those surrounded by a tenuous disc, and those with no detectable infrared excess (i.e., bare photospheres). Inspecting the computed SEDs we find several of these objects within the Class III of our sample. Therefore we applied an extra classification based on the infrared slope between  $\sim 12 \mu\text{m}$  and  $\sim 22 \mu\text{m}$  ( $\alpha_{\text{W34}}$ ). We classify as bare photospheres the Class III objects with  $\alpha_{\text{W34}} < -1.6$ , and reclassify the Class III objects as those with  $\alpha_{\text{W34}} > -1.6$  and  $\alpha_{\text{IR}} < -1.6$ . Using this classification scheme we identify 7 bare photospheres and 5 Class III sources, as reflected in Fig. 11. Therefore, we find a disc fraction of  $\sim 85\%$  in this subsample of 48 objects. Bearing in mind the strong selection biases of our sample, we note that this high disc fraction is consistent with an age of  $\sim 2$  Myr according to different studies (e.g., Ribas et al. 2015; Fedele et al. 2010; Mamajek 2009). A table with the photometry for these 48 objects is given in the Appendix (Table .4) and it will be available in the electronic version of this document. This table contains a “status” keyword that indicates if a disc is included in the control sample (labelled as “control”), or if the disc has currently no references in the SIMBAD service (labelled as “new”). We find 12 new discs, 11 of them with Class II SEDs and 1 of them with Class III SED (*Gaia* DR2 #6051732000945974912). The SEDs for these 12 new discs are shown in Fig. 12, and their corresponding WISE W4 images are shown in the Appendix (Fig. .5). We note that the disc around the *Gaia* DR2 #6050899361406000000 source shows the strong rising towards  $22 \mu\text{m}$  characteristic of a disc with a large dust depleted inner cavity as e.g. Sz91 (Canovas et al. 2015, 2016; Tsukagoshi et al. 2014).

## 5. Summary and conclusions

In this work we have used three density-based clustering algorithms (DBSCAN, OPTICS, and HDBSCAN) to identify potential new members of the  $\rho$ -Oph region in the *Gaia* DR2 catalogue. The members of the same SFR have similar proper motions and spatial distributions, so these Machine Learning algorithms are well suited to detect them.

We began by constructing a comprehensive sample of Ophiuchus members previously identified by Wilking et al. (2008), Erickson et al. (2011), and Dunham et al. (2015). Table .1 lists the 465 elements of this catalogue. We then used the 2MASS source IDs of these objects to cross-match them against the *Gaia* DR2 catalogue. Applying the quality selection criteria described in Sect. 2.2 and removing the outliers we obtained a control sample composed by 188 elements. This catalogue of bona fide members, which may be useful for future studies of the  $\rho$ -Oph cloud, is accessible via Table .1 through the “Control” keyword. We then downloaded the *Gaia* DR2 sources contained within a circular area of  $r = 3.5^\circ$  centred on  $\rho$ -Oph and with  $5 < \varpi < 9$ , a region large enough to encompass the entire control sample (Fig. 1). We imposed the quality selection criteria outlined in Sects. 2.2 and 2.3, and then separately applied the DBSCAN,

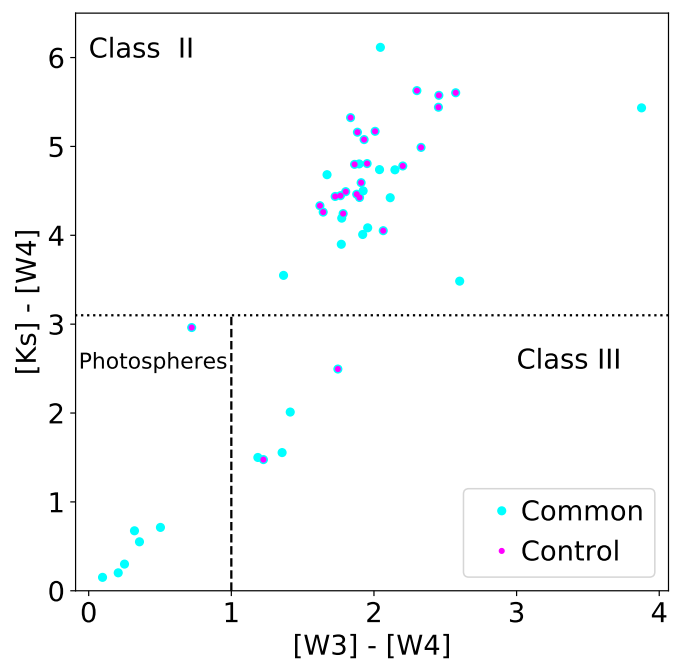


**Fig. 11.** Color-color plot of the common sample with high quality infrared photometry. The dotted line indicates the traditional boundary between the Class II and III stages. The vertical dashed line separates bare photospheres from Class III discs.

OPTICS, and HDBSCAN algorithms to the 5 astrometric dimensions ( $XYZ$  Cartesian coordinates and the proper motions  $\mu_{\alpha^*}$  and  $\mu_{\delta}$ ) of this sample. DBSCAN systematically finds one large cluster consistent with the control sample astrometric properties, while OPTICS and HDBSCAN identify two clusters, the largest of them having astrometric properties similar to those of the control sample (Fig. 6). Discussing in detail the properties of the secondary cluster is out of the scope of this paper, and we defer its analysis to a separate study. The size of this main cluster depends on the algorithm hyperparameters, ranging from 427 to 552 elements. On average, the algorithms recover  $\sim 84\%$  of the control sample as shown in Table 2. Combining the different algorithm outcomes we constructed the minimum common sample. This sample, presented in Table 3, contains 391 candidate members of  $\rho$ -Oph including 148 control sample elements and 166 sources that, to date, have no reference in the literature according to SIMBAD. 77 sources appear associated either to  $\rho$ -Oph or to Upper Sco (i.e., Cieza et al. 2007; Cheetham et al. 2015; Luhman & Mamajek 2012; Rizzuto et al. 2015). The average distance to the common sample ( $d = 139.4_{-3.8}^{+4.1}$  pc) is consistent, within error bars, with previous distance estimates towards the  $\rho$ -Oph cloud (Makarov 2007; Mamajek 2008; Ortiz-León et al. 2017, 2018).

In Sect. 4.1 we analyse the astrometric properties of the common sample. The parallax distribution is narrower than that of the control sample ranging from  $[6.7 : 7.7]$  and showing a double peak at  $\varpi = 7.0, 7.2$ . The proper motion histograms show double Gaussian-like profiles with main and secondary peaks at  $-6.9 \pm 0.1$  and  $-10.4 \pm 0.5$  in  $\mu_{\alpha^*}$ , and  $-25.4 \pm 0.1$  and  $-21.6 \pm 0.1$  in  $\mu_{\delta}$  (Figs. 8 and 9, and Table 4). The extinction uncorrected color magnitude diagram is shown in Fig. 10 and discussed in Sect. 4.2. The CMD suggests that the common sample is dominated by objects younger than 5 Myr with masses below  $0.5 M_{\odot}$ , in agreement with previous studies of this cloud (Wilking et al. 2005; Erickson et al. 2011), but we are cautious about our con-

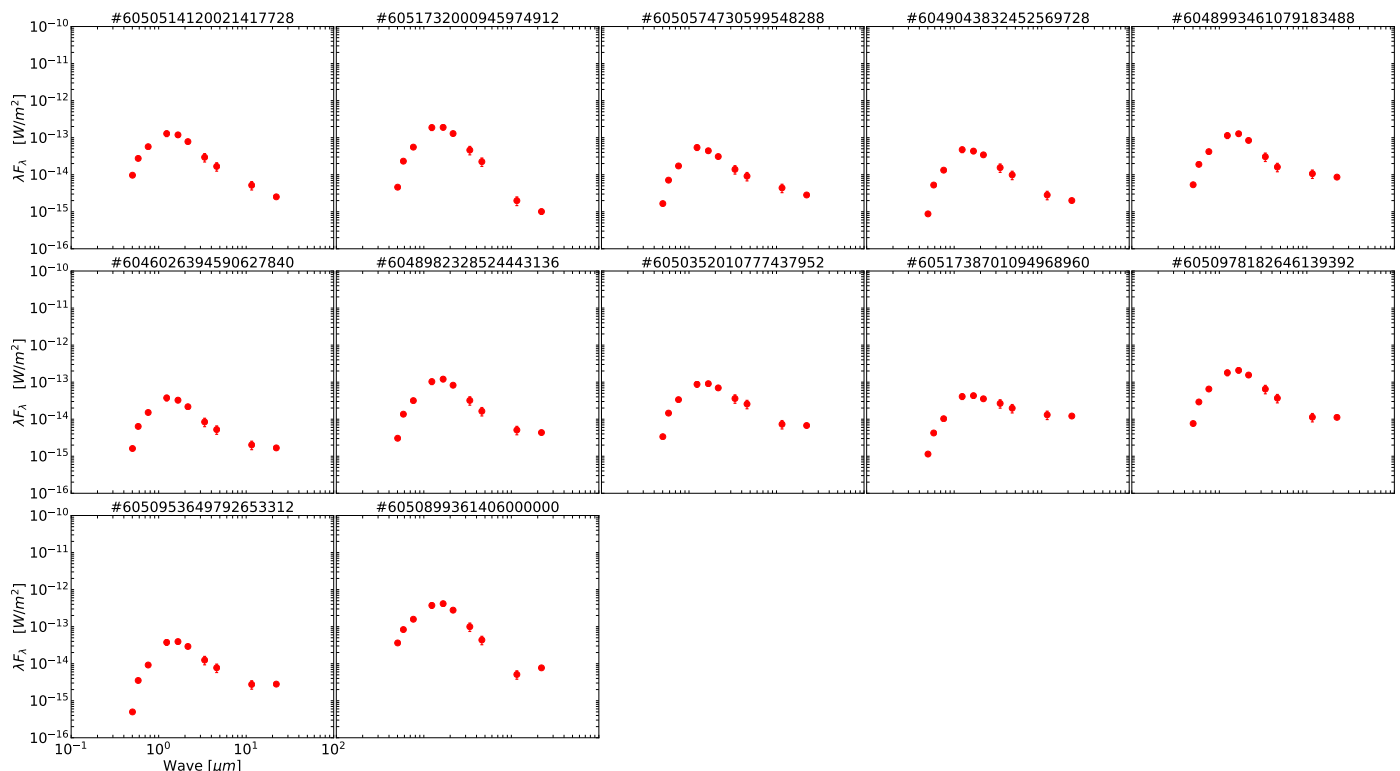


**Fig. 12.** SEDs of the 12 new discs detected. The title indicates the *Gaia* DR2 source ID. The panels are ordered by increasing  $\alpha_{W34}$  slope. Object #6051732000945974912 is the only Class III disc of this subsample, as the rest are Class II discs. Source #605089936140600000 shows the characteristic SED shape of a disc with a dust depleted inner cavity.

clusions given the large uncertainty associated to the (yet unknown) extinction of these sources. Finally, in Sect. 4.3 we constructed the SEDs from optical to mid-infrared wavelengths for the subset of 48 objects with high quality photometry in the *Gaia*, 2MASS, and WISE bands. Applying a color selection criteria (Fig. 11) we identify 36 Class II, 5 Class III objects, and 7 bare photospheres. Their photometry, along with their SED Class and a flag indicating if the object has no references in SIMBAD, is given in Table .4. Twelve of these objects have no references on the SIMBAD service and show strong infrared emission, and their SEDs are shown in Fig. 12. Their corresponding WISE W4 maps are presented in Fig .5.

This work reflects the potential of applying modern Machine Learning techniques to identify young stellar populations in huge astronomical catalogues such as the *Gaia* DR2. These tools are specially useful when the region under study is affected by a high extinction that hinders a sample selection from a color magnitude diagram (as in e.g., Goldman et al. 2018). However, we are aware of a number of limitations of our study. To begin with, none of the algorithms here discussed takes into account the measurement uncertainties and, as shown through our analysis, the outcomes are sensitive to the hyperparameters given by the user. We have attempted to overcome these issues by combining the results of the three algorithms and focusing our analysis in the minimum size common sample of the multiple cases listed in Table 2. Another caveat to consider is that star forming regions are very complex environments and a fraction of their components might not be located in a cloud core but in a stream or filament-like spatial structure (André et al. 2010). This is indeed the case for  $\rho$ -Oph, with at least two prominent filaments that seem to depart from the L1688 dark cloud (Ridge et al. 2006). This complex spatial distribution makes it more difficult for the clustering algorithms to identify the cloud members, and

that can explain why the applied algorithms did not recover the entire control sample but  $\sim 80\%$  of it. This can also explain the narrow range in the parallax distribution of the common sample when compared to that of the control sample. A third important caveat is that, given the proximity in terms of parallax and coordinates, it is possible that a fraction of the stars in our sample was formed in the 5 – 10 Myr old Upper Sco region (Mamajek 2008; Wilking et al. 2005, 2008). The fact that 43 members of the common sample have been associated to Upper Sco is an indicative of this possible contamination. A potential way to discern the nature of these sources would be to analyse the radial velocities, which we have not included in our study given the lack of measurements in the *Gaia* DR2. Future data releases are expected to include more radial velocity measurements and therefore will become ideal catalogues to repeat studies like this one. In the meantime, the brighter objects of the common sample could be followed-up with spectroscopy in order to determine their effective temperatures and extinctions, and therefore to estimate their ages and masses (which would also help to constraint their parental region).

It is not surprising that none of the studied objects with infrared photometry belongs to the earlier Class 0, and I stages. These objects are very embedded and extinct, and therefore they are relatively difficult targets for *Gaia*. The 12 discs that we have discovered are good candidates to be directly imaged at optical and near infrared wavelengths with high-contrast instruments like SPHERE (Beuzit et al. 2008) at the Very Large Telescopes (VLT), and at sub-millimeter and longer wavelengths with the ALMA observatory. Given the high fraction of circumstellar discs that we found in our subset of 48 targets ( $\sim 85\%$ ), the objects here discussed lacking infrared photometry are promising targets to search for discs with future infrared facilities like the James Webb Space Telescope (JWST) and/or proposed mis-

sions like the Space Infrared Telescope for Cosmology and Astrophysics (SPICA).

*Acknowledgements.* H.C. gratefully acknowledges support from the European Space Agency (ESA) Research Fellow program. C.C. was supported by the 2018 ESAC trainee program. L.C. was supported by CONICYT-FONDECYT grant number 1171246.

This publication makes use of data products from:

1) the Two Micron All Sky Survey, which is a joint project of the University of Massachusetts and the Infrared Processing and Analysis Center/California Institute of Technology, funded by the National Aeronautics and Space Administration and the National Science Foundation;

2) the Wide-field Infrared Survey Explorer, which is a joint project of the University of California, Los Angeles, and the Jet Propulsion Laboratory/California Institute of Technology, funded by the National Aeronautics and Space Administration.

3) the European Space Agency (ESA) mission *Gaia* (<https://www.cosmos.esa.int/gaia>), processed by the *Gaia* Data Processing and Analysis Consortium (DPAC, <https://www.cosmos.esa.int/web/gaia/dpac/consortium>). Funding for the DPAC has been provided by national institutions, in particular the institutions participating in the *Gaia* Multilateral Agreement.

This research has made use of:

1) the NASA/ IPAC Infrared Science Archive, which is operated by the Jet Propulsion Laboratory, California Institute of Technology, under contract with the National Aeronautics and Space Administration;

2) the VizieR catalogue access tool, CDS, Strasbourg, France; and

3) Astropy, a community-developed core Python package for Astronomy Astropy Collaboration 2013.

## References

- Andrae, R., Fouesneau, M., Creevey, O., et al. 2018, *A&A*, 616, A8
- André, P., Men'shchikov, A., Bontemps, S., et al. 2010, *Astronomy and Astrophysics*, 518, L102
- Andrews, S. M., Rosenfeld, K. A., Kraus, A. L., & Wilner, D. J. 2013, *ApJ*, 771, 129
- Andrews, S. M. & Williams, J. P. 2007, *ApJ*, 671, 1800
- Andrews, S. M., Wilner, D. J., Hughes, A. M., Qi, C., & Dullemond, C. P. 2009, *ApJ*, 700, 1502
- Ankerst, M., Breunig, M. M., Kriegel, H.-P., & Sander, J. 1999, in *Proceedings of the 1999 ACM SIGMOD International Conference on Management of Data, SIGMOD '99* (New York, NY, USA: ACM), 49–60
- Ansdell, M., Williams, J. P., Manara, C. F., et al. 2017, *AJ*, 153, 240
- Ansdell, M., Williams, J. P., van der Marel, N., et al. 2016, *ApJ*, 828, 46
- Arenou, F., Luri, X., Babusiaux, C., et al. 2018, *A&A*, 616, A17
- Bailer-Jones, C. A. L. 2015, *PASP*, 127, 994
- Baraffe, I., Homeier, D., Allard, F., & Chabrier, G. 2015, *A&A*, 577, A42
- Bate, M. R. 2011, *Monthly Notices of the Royal Astronomical Society*, 419, 3115
- Bate, M. R. 2018, *Monthly Notices of the Royal Astronomical Society*, 475, 5618
- Beccari, G., Boffin, H. M. J., Jerabkova, T., et al. 2018, *Monthly Notices of the Royal Astronomical Society: Letters*, 481, L11
- Beuzit, J.-L., Feldt, M., Dohlen, K., et al. 2008, in *Society of Photo-Optical Instrumentation Engineers (SPIE) Conference Series*, Vol. 7014, *Society of Photo-Optical Instrumentation Engineers (SPIE) Conference Series*, 18
- Bianchini, P., van der Marel, R. P., del Pino, A., et al. 2018, *Monthly Notices of the Royal Astronomical Society*, 481, 2125
- Brown, A. G. A., Vallenari, A., Prusti, T., et al. 2016, *Astronomy & Astrophysics*, 595, A2
- Brown, A. G. A., Vallenari, A., Prusti, T., et al. 2018, *Astronomy & Astrophysics*, 616, A1
- Bruijne, J. H. J. d. 1999, *Monthly Notices of the Royal Astronomical Society*, 306, 381
- Caballero, J. A. & Dinis, L. 2008, *Astronomische Nachrichten*, 329, 801
- Campello, R. J. G. B., Moulavi, D., & Sander, J. 2013, in *Advances in Knowledge Discovery and Data Mining*, ed. J. Pei, V. S. Tseng, L. Cao, H. Motoda, & G. Xu (Berlin, Heidelberg: Springer Berlin Heidelberg), 160–172
- Campello, R. J. G. B., Moulavi, D., Zimek, A., & Sander, J. 2015, 10, 1
- Canovas, H., Cáceres, C., Schreiber, M. R., et al. 2016, *MNRAS*, 458, L29
- Canovas, H., Schreiber, M. R., Cáceres, C., et al. 2015, *ApJ*, 805, 21
- Castro-Ginard, A., Jordi, C., Luri, X., et al. 2018, *Astronomy & Astrophysics*, 618, A59
- Cheetham, A. C., Kraus, A. L., Ireland, M. J., et al. 2015, *The Astrophysical Journal*, 813, 83
- Cieza, L., Padgett, D. L., Stapelfeldt, K. R., et al. 2007, *ApJ*, 667, 308
- Cieza, L. A., Ruíz-Rodríguez, D., Hales, A., et al. 2018, *Monthly Notices of the Royal Astronomical Society*, 482, 698
- Costado, M. T., Alfaro, E. J., González, M., & Sampedro, L. 2017, *MNRAS*, 465, 3879
- Cox, E. G., Harris, R. J., Looney, L. W., et al. 2017, *ApJ*, 851, 83
- Cuello, N., Dipierro, G., Mentiplay, D., et al. 2019, *MNRAS*, 483, 4114
- de Zeeuw, P. T., Hoogerwerf, R., de Bruijne, J. H. J., Brown, A. G. A., & Blaauw, A. 1999, *AJ*, 117, 354
- Dent, W. R. F., Thi, W. F., Kamp, I., et al. 2013, *Publications of the Astronomical Society of the Pacific*, 125, 477
- Dunham, M. M., Allen, L. E., Evans II, N. J., et al. 2015, *The Astrophysical Journal Supplement Series*, 220, 11
- Erickson, K. L., Wilking, B. A., Meyer, M. R., Robinson, J. G., & Stephenson, L. N. 2011, *AJ*, 142, 140
- Ester, M., Kriegel, H.-P., Sander, J., & Xu, X. 1996, in *Proceedings of the Second International Conference on Knowledge Discovery and Data Mining, KDD'96* (AAAI Press), 226–231
- Evans, II, N. J., Allen, L. E., Blake, G. A., et al. 2003, *PASP*, 115, 965
- Evans, II, N. J., Dunham, M. M., Jørgensen, J. K., et al. 2009, *ApJS*, 181, 321
- Fedele, D., van den Ancker, M. E., Henning, T., Jayawardhana, R., & Oliveira, J. M. 2010, *A&A*, 510, A72
- Feigelson, E. D. & Babu, G. J. 2012, *Modern Statistical Methods for Astronomy*
- Gagné, J., Mamajek, E. E., Malo, L., et al. 2018, *ApJ*, 856, 23
- Gaia Collaboration, Prusti, T., de Bruijne, J. H. J., et al. 2016, *A&A*, 595, A1
- Goldman, B., Röser, S., Schilbach, E., Moór, A. C., & Henning, T. 2018, *ApJ*, 868, 32
- Greene, T. P., Wilking, B. A., Andre, P., Young, E. T., & Lada, C. J. 1994, *ApJ*, 434, 614
- Hague, P. R., Ye, H., Nikolic, B., & Gull, S. F. 2019, *MNRAS*, 484, 574
- Haisch, Jr., K. E., Lada, E. A., & Lada, C. J. 2001, *ApJ*, 553, L153
- Jarrett, T. H., Cohen, M., Masci, F., et al. 2011, *The Astrophysical Journal*, 735, 112
- Joncour, I., Duchêne, G., Moraux, E., & Motte, F. 2018, *Astronomy & Astrophysics*, 620, A27
- Katz, H., Lelli, F., McGaugh, S. S., et al. 2017, *MNRAS*, 466, 1648
- Kennedy, G. M. & Wyatt, M. C. 2012, *MNRAS*, 426, 91
- Kimm, T., Haehnelt, M., Blaizot, J., et al. 2018, *MNRAS*, 475, 4617
- Knuth, K. H. 2006, *ArXiv Physics e-prints [physics/0605197]*
- Kraus, A. L. & Hillenbrand, L. A. 2007, *The Astrophysical Journal*, 662, 413
- Lada, C. J. 1987, in *IAU Symposium*, Vol. 115, *Star Forming Regions*, ed. M. Peimbert & J. Jugaku, 1–17
- Lada, C. J. & Wilking, B. A. 1984, *ApJ*, 287, 610
- Lindgren, L., Hernández, J., Bombrun, A., et al. 2018, *Astronomy & Astrophysics*, 616, A2
- Lindgren, L., Lammers, U., Hobbs, D., et al. 2012, *Astronomy & Astrophysics*, 538, A78
- Lloyd, S. P. 1982, *IEEE Transactions on Information Theory*, 28, 129
- Lombardi, M. & Alves, J. 2001, *A&A*, 377, 1023
- Luhman, K. L. & Mamajek, E. E. 2012, *ApJ*, 758, 31
- Makarov, V. V. 2007, *ApJS*, 169, 105
- Malo, L., Doyon, R., Lafrenière, D., et al. 2013, *ApJ*, 762, 88
- Mamajek, E. 2008, *Astronomische Nachrichten*, 329, 10
- Mamajek, E. E. 2009, in *American Institute of Physics Conference Series*, Vol. 1158, *American Institute of Physics Conference Series*, ed. T. Usuda, M. Tamura, & M. Ishii, 3–10
- Marigo, P., Girardi, L., Bressan, A., et al. 2017, *The Astrophysical Journal*, 835, 77
- McInnes, L., Healy, J., & Astels, S. 2017, *The Journal of Open Source Software*, 2
- Merín, B., Brown, J. M., Oliveira, I., et al. 2010, *ApJ*, 718, 1200
- Montmerle, T., Koch-Miramond, L., Falgarone, E., & Grindlay, J. E. 1983, *ApJ*, 269, 182
- Morbidelli, A. & Raymond, S. N. 2016, *Journal of Geophysical Research (Planets)*, 121, 1962
- Novikov, A. 2018, *annoviko/pyclustering: pyclustering 0.8.1 release*
- Ortiz-León, G. N., Loinard, L., Dzib, S. A., et al. 2018, *ApJ*, 869, L33
- Ortiz-León, G. N., Loinard, L., Kounkel, M. A., et al. 2017, *ApJ*, 834, 141
- Osuna, P., Ortiz, I., Lusted, J., et al. 2008, *IVOA Astronomical Data Query Language Version 2.00*, *IVOA Recommendation* 30 October 2008
- Pascucci, I., Testi, L., Herczeg, G. J., et al. 2016, *ApJ*, 831, 125
- Pedregosa, F., Varoquaux, G., Gramfort, A., et al. 2011, *Journal of Machine Learning Research*, 12, 2825
- Ribas, Á., Bouy, H., & Merín, B. 2015, *A&A*, 576, A52
- Ridge, N. A., Di Francesco, J., Kirk, H., et al. 2006, *AJ*, 131, 2921
- Rizzuto, A. C., Ireland, M. J., & Kraus, A. L. 2015, *MNRAS*, 448, 2737
- Robitaille, T. P., Tollerud, E. J., Greenfield, P., et al. 2013, *Astronomy & Astrophysics*, 558, A33
- Rodrigo, C., Solano, E., & Bayo, A. 2012, *SVO Filter Profile Service Version 1.0*, *IVOA Working Draft* 15 October 2012

- Ruíz-Rodríguez, D., Cieza, L. A., Williams, J. P., et al. 2018, *Monthly Notices of the Royal Astronomical Society*, 478, 3674
- Sans Fuentes, S. A., De Ridder, J., & Debosscher, J. 2017, *A&A*, 599, A143
- Skrutskie, M. F., Cutri, R. M., Stiening, R., et al. 2006, *AJ*, 131, 1163
- Taylor, M. 2017, ArXiv e-prints [arXiv:1707.02160]
- Tramacere, A. & Vecchio, C. 2013, *Astronomy & Astrophysics*, 549, A138
- Tsukagoshi, T., Momose, M., Hashimoto, J., et al. 2014, *ApJ*, 783, 90
- Walter, F. M., Vrba, F. J., Mathieu, R. D., Brown, A., & Myers, P. C. 1994, *The Astronomical Journal*, 107, 692
- Wenger, M., Ochsenbein, F., Egret, D., et al. 2000, *A&AS*, 143, 9
- Wilking, B. A., Gagné, M., & Allen, L. E. 2008, *Star Formation in the  $\rho$  Ophiuchi Molecular Cloud*, ed. B. Reipurth, 351
- Wilking, B. A., Meyer, M. R., Robinson, J. G., & Greene, T. P. 2005, *AJ*, 130, 1733
- Wilking, B. A., Schwartz, R. D., & Blackwell, J. H. 1987, *AJ*, 94, 106
- Wilkinson, S., Merín, B., & Riviere-Marichalar, P. 2018, *A&A*, 618, A12
- Wright, E. L., Eisenhardt, P. R. M., Mainzer, A. K., et al. 2010, *The Astronomical Journal*, 140, 1868

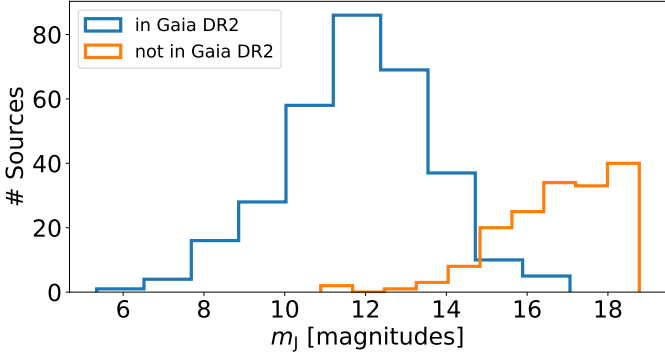


**Fig. .1.** Apparent  $J$  band magnitude histograms of the initial sample.

2MASS ID	$\varpi$ [mas]	$\mu_{\alpha^*}$ [mas yr $^{-1}$ ]	$\mu_{\delta}$ [mas yr $^{-1}$ ]
16293441-2452292	8.9451	-37.9989	-118.5701
16442882-2412242	2.1726	-1.8833	-5.9312
16245652-2459381	1.4977	-7.6758	-3.7136
16265752-2446060	10.2548	56.4965	-59.1305
16282516-2445009	13.1651	-52.7356	-62.1384
16244802-2440051	38.5067	-85.4146	-152.0051
16260302-2423360	7.4456	-20.1836	-26.7646
16273052-2432347	9.3827	84.3542	-41.9827
16273714-2359330	2.0953	4.7860	4.0732

**Table .2.** Objects excluded from the control sample. They appear as outliers on the bell-shaped histograms shown in Fig. .2.

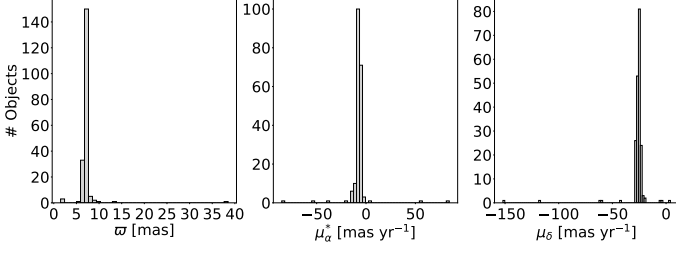


**Fig. .2.** Parallax and proper motion histograms of the astrometrically cleaned sample. Note the few outliers located far away from the histogram peaks.

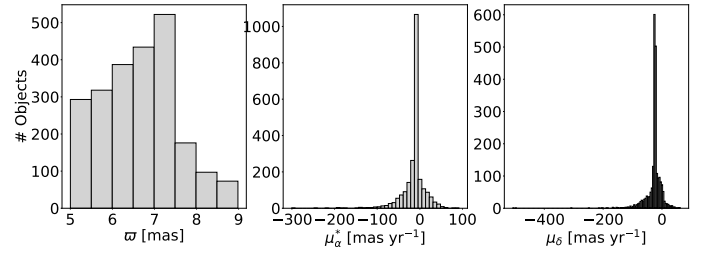


**Fig. .4.** Same as Fig. .2 but for the *Gaia* cleaned sample.

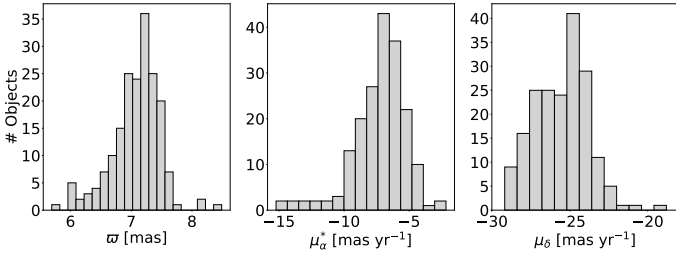


**Fig. .3.** Same as Fig. .2 but for the control sample (obtained after removing the the outliers listed in Table .2 from the astrometrically cleaned sample).

2MASS	Refs.	Control	DR2 Source ID
16261949-2437275	1, 2, 3	Y	6049122310095142656
16262083-2428395	1, 3	N	
16262096-2408468	3	Y	6049357429490158336
16262097-2408518	1, 2	Y	6049357433785068672
16262138-2423040	1, 3	N	

**Table .1.** Extract of the initial sample presented in Sect. 2.1. The entire table will be listed in the electronic version of the accepted article. References are coded as 1: Wilking et al. (2008), 2: Erickson et al. (2011), and 3: Dunham et al. (2015). Note: 5 targets have duplicate *Gaia* source\_id: 2MASS J16222099-2304025, 2MASS J16233609-2402209, 2MASS J16253958-2426349, 2MASS J16275565-2444509, and 2MASS J16282373-2441412. These duplicates are removed when applying the selection criteria described in Sect. 2.2, but we keep them in the table for consistency.

DR2 Source ID	Ref.	$A_V$ mag	$A_G$ mag
6046062364938324608	1	4.2	0.8
6047590243721186688	1	4.4	2.6
6049067776894321024	1	3.9	1.3
6049094616145974272	1	6.3	2.2
6049095406419962112	1	7.9	1.9
6049101866050768384	1	2.9	1.9
6049118388788178816	1	4.0	2.8
6049122310095142656	1	1.6	2.2
6049142410542091648	1	4.5	2.8
6049161514556593920	1	15.9	2.0
6049162545348745984	1	10.8	2.1
6049331526542488064	1	6.6	2.0
6049367398109200256	1	6.3	1.4
6050172068822858624	1	0.0	0.7
6050204641855013376	1	3.9	1.3
6050345001390940160	2	0.6	0.8
6050487456864139392	2	0.9	1.6
6050626201483958400	1	2.0	2.3
6050644102907664640	1	1.9	0.9
6050681211424993280	1	4.3	2.1
6051734990243252096	1	2.2	1.9
6051764573978499200	2	0.8	0.9

**Table .3.** Objects in the common sample with published  $A_V$  and *Gaia* DR2  $A_G$  values (see Sect. 4.2). References are coded as (1): Dunham et al. (2015), (2): Rizzuto et al. (2015).

DR2 Source ID	GFlux Jy	GbFlux Jy	GrFlux Jy	JFlux Jy	HFlux Jy	KsFlux Jy	W1Flux Jy	W2Flux Jy	W3Flux Jy	W4Flux Jy	SED_Class	status
6244269200073741312	0.824753	0.736159	1.097934	1.158963	0.924301	0.639969	0.315541	0.174455	0.029112	0.008415	Photosphere	
6050352659313505536	2.963747	3.251110	2.946513	2.333832	1.575483	1.042699	0.490067	0.271696	0.044923	0.014370	Photosphere	
6049011053265501056	1.616139	1.322244	2.398870	3.404627	2.880141	2.231304	1.160528	0.702882	0.101034	0.033656	Photosphere	
6050895783696207872	0.045971	0.024306	0.094707	0.243484	0.292021	0.240192	0.124582	0.070094	0.013362	0.004602	Photosphere	New
6051097681519794944	0.099691	0.057391	0.190973	0.419247	0.487769	0.388471	0.187178	0.105897	0.021911	0.008640	Photosphere	
6049107428032112384	0.026920	0.006688	0.075927	0.509178	1.040911	1.210483	1.007271	1.132356	0.442861	0.213650	Photosphere	Control
6052114802793345792	1.106760	1.117204	1.258947	1.170765	0.826825	0.578840	0.280708	0.156777	0.036809	0.028972	Class III	
6049286687085135360	0.313597	0.220962	0.529386	0.890573	0.773061	0.613986	0.353717	0.191462	0.036843	0.030060	Class III	Control
6050496459111584384	0.797635	0.756984	0.988171	0.969326	0.706340	0.511633	0.247432	0.137430	0.029265	0.026939	Class III	
6050514120021417728	0.005357	0.001622	0.014426	0.052926	0.065859	0.056307	0.033082	0.025690	0.020024	0.018603	Class II	New

**Table .4.** Extract from the photometry table. This entire table will be available on the electronic version of this document.

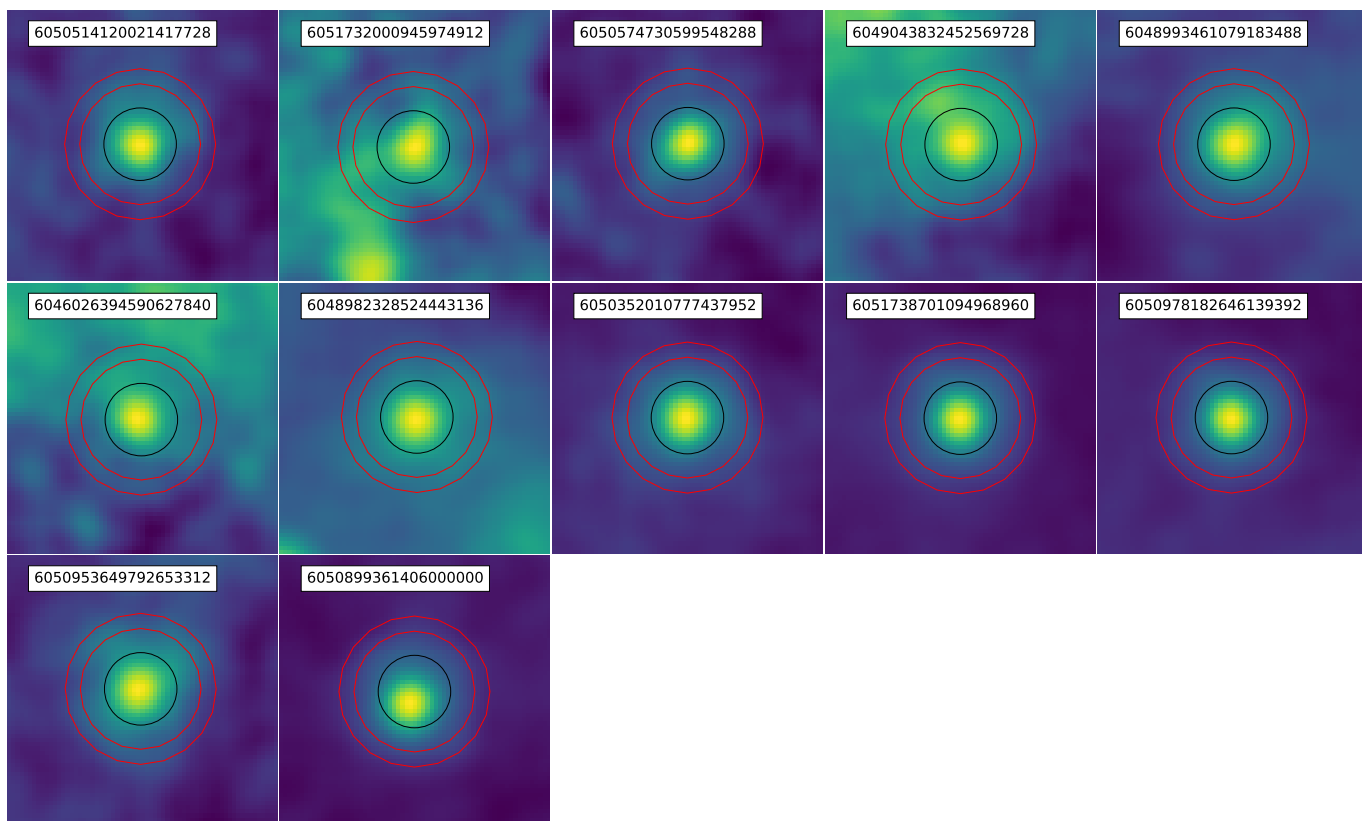


**Fig. .5.** WISE W4 maps of the 12 new discs shown in Fig. 12. The black line encompasses the aperture mask used to find the emission peak associated to the disc ( $r = 12''$ ), and the red lines indicate the ring area used to estimate the background emission ( $r_{in} = 20''$ ,  $r_{out} = 25''$ , see Sect. 4.3). All the images are  $1.5' \times 1.5'$  in size, and the white panels indicate the *Gaia* DR2 source ID.